Martensitic transformation of SS304 truncated square pyramid manufactured by single point incremental forming

by

Elizabeth M. Mamros[a]*, Fabian Maaß[b], A. Erman Tekkaya[b], Brad L. Kinsey[c], Jinjin Ha[c]

* Corresponding author: elizabeth.mamros@bucknell.edu

July 2024

[a] Department of Mechanical Engineering, Bucknell University, Lewisburg, PA 17837, USA

[b] Institute of Forming Technology and Lightweight Components, TU Dortmund University, 44227 Dortmund, Germany

[c] Department of Mechanical Engineering, University of New Hampshire, Durham, NH 03824, USA

Abstract

To investigate the microstructural changes that occur in stainless steel (SS) 304 during single point incremental forming (SPIF), experiments and finite element (FE) simulations were conducted for a truncated square pyramid geometry. Results from material characterization experiments for four stress states, i.e., uniaxial tension, equibiaxial tension, shear, and uniaxial compression, were combined to construct a material model based on the constituent phases and transformation kinetics. The material model was implemented into numerical analyses, where a two-step FE approach was utilized to predict martensite transformation in SPIF with increased computational efficiency. Validation experiments showed good agreement with the martensite transformation predictions from the FE simulations. The four locations along the pyramid wall revealed varying martensite volume fractions because of the differing stress states of bending, stretching, and shear that the blank is subjected to during SPIF, which can affect the microstructure. The stress state can be defined in terms of the stress triaxiality and Lode angle parameter. The FE results indicate that stress triaxiality impacted the martensitic transformation kinetics in SS304 more than the Lode angle parameter for SPIF for this particular material and geometry. Thus, distinct stress states in incremental forming can affect the martensitic transformation locally and, when used strategically, achieve functionally graded materials. This is pertinent to industrial applications requiring custom components, e.g., trauma fixation hardware for medical applications.

Keywords: Stainless steel, single point incremental forming, martensite transformation, stress triaxiality, Lode angle parameter

1. Introduction

Incremental forming is a flexible, sustainable manufacturing process that conventionally uses one tool, known as single point incremental forming (SPIF), to locally deform clamped sheet metal blanks, layer by layer, into complex geometries [1]. Since it is a dieless process, incremental forming does not require specialized equipment and can be performed in industrial settings with a ubiquitous computer numerical control (CNC) milling machine [2] or robotics [3]. Incremental forming is ideal for rapid prototyping applications because the toolpath and process parameters can be adjusted to achieve mass-customization and influence the final part properties [4]. One review hypothesizes that there is an optimal range for each parameter and undetermined relationships among the parameters [5]. Incremental forming is a cost-saving, safe, and environmentally friendly alternative to the other rapid prototyping methods, such as powder-based metal additive manufacturing, which emits volatile organic compounds during the process and requires expensive equipment [6].

One of the critical advantages of SPIF, compared to traditional sheet metal forming processes, including stamping using servo motors [7,8], is increased material formability. This enhanced formability is largely due to the combination of bending and in plane stresses enabled by localized plastic deformation inherent to the process [9–11]. To decrease the computational expense require to assess this phenomenon, simulations of a paddle forming process were compared to SPIF experiments for a truncated square pyramid [12]. More recent studies have shifted their focus to understand the material failure mechanisms of SPIF, and two of these theories are summarized in [13].

Tisza provides a brief overview of the history of SPIF in [14]. In 1967, Leszak Edward patented the incremental dieless forming process [15]. Interest in this manufacturing process, which used localized deformation to produce complex geometries with CNC machining centers, escalated quickly. Incremental forming showed immense promise as a means of rapid prototyping with sheet metal [16]. Recently, dedicated machines with additional loading capabilities have been fabricated for incremental forming to further explore the possibilities of this technology. Many variations on the SPIF process and process parameters have been implemented. Several studies have considered using different tools, such as a roller-ball tool to decrease friction [17] or multi-directional tooling to increase formability, improve the surface finish, and reduce springback [18]. In addition to different types of tooling, investigations of electrically-assisted incremental forming processes using aluminum alloys, e.g., 6061-T6 [19] and 2023-T3 [20], and high strength steel [21] have been conducted. To successfully form parts from aluminized sheets pre-coated with polytetrafluoroethylene, Rodriguez-Alabanda and Guerrero-Vaca introduced the use of a sacrificial sheet during forming to preserve the part's coating and found improved hydrophobicity resulting from the elastic-plastic deformation during SPIF [22]. Hassan et al. conducted numerical simulations, comparing three different damage models, and validation experiments for pressure-assisted SPIF, which uses a pressurized fluid to provide support opposite of the forming tool [23]. The toolpath design, which is essential to making incremental forming a suitable process for highly customized parts, has been the subject of many studies and continues to be an active research topic. Maaß et al. considered how the toolpath strategy affects the residual stress development in aluminum alloy 5083 [24]. Rashid et al. concluded from

the Taguchi approach that the tool diameter and selected wall angle were the most critical parameters affecting the residual stresses in an asymmetrical truncated pyramid part [25]. Another study focused on reducing springback by erecting formed stiffeners around the part [26]. Toolpath strategies have also been investigated, including multi-pass SPIF, where intermediate geometries are formed prior to the target geometry [27]. One process variant that is gaining traction is double-sided incremental forming (DSIF), which introduces an independently controlled support tool on the opposite side of the sheet. DSIF requires a more sophisticated equipment setup, either a custom machine or two robots, but the process can create more complex geometries, such as undercuts, which are not possible with SPIF, and, generally, greater geometrical accuracy [28]. Recently, a study introduced multiple support tools, so-called double-side multi-point incremental forming, and the use of electricity during this forming process [29]. Darzi et al. investigated the temperature and deformation path effect on martensite transformation of SS304L sheet in DSIF [30,31].

In SPIF, three deformation modes occur, bending, tension, and shear, which lead to different stress states. The composition of these three modes can be controlled by the process parameters such as the tool radius and stepdown increment, as shown in [32], and ultimately affect the residual stresses. Maqbool and Bambach developed an analytical approach that uses the plastic energy terms from SPIF simulations to determine the contributions of each of the three deformation modes at different intervals [33]. Kim and Park [34] investigated how tool type, tool size, feed rate, friction, and material planar anisotropy affected formability. To better understand why SPIF leads to formability beyond the forming limit used for other manufacturing processes [35,36], five parameters

have been proposed in [37]: contact stress, bending under tension, shear, cyclic straining, and geometrical inability to grow necks. More recently, studies have pivoted to investigate how microstructural changes influence the increased formability resulting from SPIF. To focus on the role of stress triaxiality in formability, Martínez-Donaire et al. [38] conducted hole-flanging by SPIF experiments on AA7075-O sheets. For austenitic stainless steel (SS) 301, nano-twins were formed during SPIF and resulted in increased strength and ductility during the early stages of deformation [39]. Katajarinne and Kivivuori [40] found that martensitic transformation decreased with increased forming speeds due to the increased heat generation for stainless steels. Katajarinne et al. [41] controlled the martensite transformation during SPIF by changing the process temperature using a fluid-filled container in contact with the non-toolside that could be heated or cooled depending on the desired effect on transformation.

The austenite to martensite transformation in austenitic stainless steels is a function of multiple parameters and has led to the proposition of several transformation kinetics models in the last 50 years. Olson and Cohen observed that increased martensite transformation occurs with decreased temperatures and increased plastic strain [42]. Based on these observations, they proposed a martensitic transformation kinetics law, which is a function of temperature and equivalent plastic strain, by fitting SS304 experimental data from [43]. Later, Stringfellow et al. [44] proposed an amendment to the Olson and Cohen 1975 model [45] to include stress triaxiality as a parameter based on data from [46]. To account for the effect of strain rate on martensitic transformation kinetics, Tomita and Iwamoto [47] proposed a modified version of the Stringfellow et al. 1992 model. More recently, the influence of the stress state, which is defined by the stress

triaxiality and Lode angle parameter, on the austenite to martensite transformation has been included in a model by Beese and Mohr [48].

In addition to the transformation kinetics modeling effort, several methods have been explored to measure the α'-martensite volume fraction in stainless steel experimentally, as summarized in [49]. Recently, the use of a Feritscope has gained popularity due to its non-destructive, quick measuring capability through the detection of changes in magnetic permeability [50]. The Feritscope uses a probe to induce a magnetic field through a volume of the material [51]. The magnetic phases in the material, e.g., α'-martensite, interact with the magnetic field and output a voltage to the device. This output signal is then converted from ferrite content to α'-martensite using the conversion factor determined in, e.g., [52]. Note that measurement errors can occur if the specimen is under load, the so-called Villari effect, which results in an underestimation of the martensite volume fraction [53]. This concern can be negated by unloading and measuring specimens after testing.

In this work, the mechanical behavior of SS304 sheets was characterized by uniaxial tension, bulge, in-plane torsion, and uniaxial compression experiments (Section 2). Parameters were identified for isotropic hardening of constituent phases, i.e., γ-austenite and α'-martensite, and martensitic transformation kinetics models (Section 3), which were used in the numerical analyses (Section 4). The geometrical accuracy and martensite transformation of truncated square pyramids manufactured by SPIF were compared between experiments and finite element (FE) simulations (Section 5). In depth analyses of simulations showed that the stress triaxiality had a larger effect on the martensite transformation than the Lode angle parameter for this particular material and

geometry. Variations in the amount of martensite transformation occurring at different locations along the pyramid walls indicate that a functionally graded component was achieved. These results also support that stress state control is a sustainable, valid, and effective method for varying the microstructure to attain the desired mechanical properties.

2. Material characterization

To characterize the SS304 sheets with 0.8 mm thickness used in this investigation, uniaxial tension (Section 2.1), bulge test (Section 2.2), in-plane torsion (Section 2.3), and uniaxial compression (Section 2.4) experiments were conducted using the geometries shown in Figure 1. At least three repetitions were conducted for each test condition to confirm repeatability. The chemical composition provided by the material supplier is shown in Table 1. A stereo type digital image correlation (3D-DIC) system, ARAMIS 5M (GOM Metrology), was used to measure the strain *in situ* for the uniaxial tension, bulge test, and in-plane torsion experiments. The facet size and point distance were the default values of 19 pixels and 16 pixels, respectively.

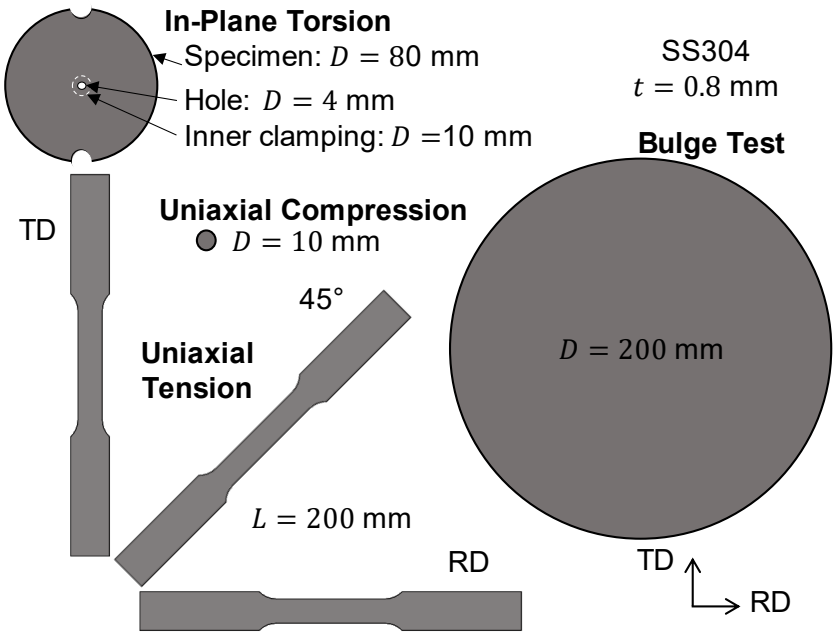

Figure 1. Specimen layout for material characterization experiments: uniaxial tension, uniaxial compression, bulge test, and in-plane torsion.

Table 1. Supplier provided chemical composition of stainless steel 304.

%C	%Si	%Mn	%P	%S	%Cr	%Ni	%Fe
0.07	1.00	2.00	0.045	0.030	17.00-19.5	8.50-10.50	Bal.

2.1 Uniaxial tension

Uniaxial tension experiments were conducted using a ZwickRoell universal testing machine with a 250 kN load cell. The ASTM E8 standard sheet-type specimen geometry [54] was used, and the displacement rates were prescribed according to ISO 6892-1 [55] producing a strain rate of ~0.001 s^{-1}. Three specimen orientations, along the rolling direction (RD), 45° to the RD, and the transverse direction (TD), were tested. Young's Modulus along the RD was determined to be approximately 170 GPa from the experimental data, and Poisson's ratio was assumed to be the textbook value of 0.33

[56]. The resulting true stress-strain curve along the RD is shown in Figure 2. The results are discussed further in Section 3.1.

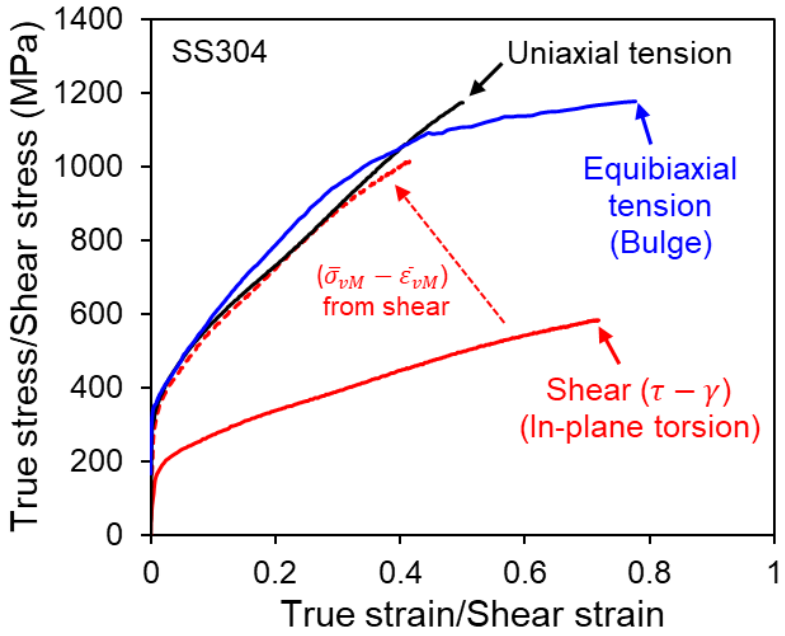

Figure 2. True stress-strain curves from uniaxial tension, equibiaxial (bulge), and shear (in-plane torsion) experiments.

2.2 Bulge test

Bulge test experiments were conducted using a ZwickRoell BUP 1000 machine and specimens with a diameter of 200 mm according to ISO 16808 [57]. The pressurizing fluid was hydraulic oil HLP 46 as specified by DIN 51524-2 [58]. The linear speed was 1.5 mm/s, and the clamping force was 1000 kN. The die opening was 120 mm in diameter and included a 4.5 mm diameter drawbead. The true stress-thickness strain curve is shown in Figure 2.

2.3 In-plane torsion

The in-plane torsion experiments were conducted using a universal testing machine with a maximum axial force of 100 kN and torque of 5000 Nm on a custom setup (Figure 3) [59]. The specimen geometry had an 80 mm diameter, and a 10 mm diameter punch was used to clamp the specimen. The center alignment hole was 4 mm in diameter. The torsional speed between the inner and outer clamping was set to 2 deg/min, which produced a strain rate of ~0.001 s^{-1}. The experiments were terminated at the onset of wrinkling, i.e., when the standard deviation of the z-coordinates located at a 7 mm radius was greater than 20% of the initial sheet thickness, as defined in [60]. The shear stress τ and strain γ are defined by:

$$\tau = \frac{M}{2\pi \cdot t \cdot r^2} \quad \text{and} \quad \gamma = \frac{d\theta}{dr}, \tag{1}$$

where M is the torque, t is the sheet thickness at the corresponding radius, r, and γ is the change in slope of a radial line on the specimen based on the angle of rotation, θ. The equivalent stress-strain curve based on von Mises (vM) assuming isotropic plastic behavior is found by:

$$\bar{\sigma}_{vM} = \sqrt{3} \cdot \tau \quad \text{and} \quad \bar{\varepsilon}_{vM} = \frac{\gamma}{\sqrt{3}}, \tag{2}$$

where $\bar{\sigma}_{vM}$ is the equivalent stress and $\bar{\varepsilon}_{vM}$ is the equivalent strain. The shear stress-strain curve for SS304 in-plane torsion and the equivalent quantity based on the von Mises yield function are shown in Figure 2.

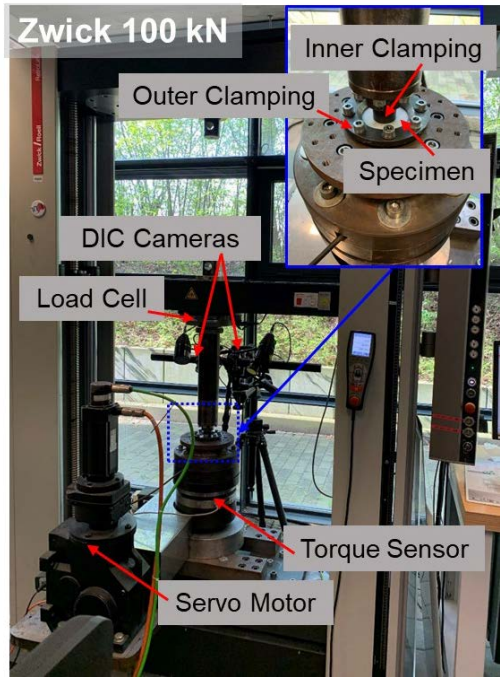

Figure 3. In-plane torsion experimental setup using 100 kN universal testing machine.

2.4 Uniaxial compression

The uniaxial compression experiments were conducted using the same machine as the uniaxial tension experiments. A Teflon spray was used to lubricate both sides of the 10 mm diameter specimens. One specimen was tested, i.e., not stacked compression tests. A displacement rate of 0.002 mm/s, equivalent to strain rate of ~0.002 s^{-1}, was prescribed, and five force levels were chosen to provide data at different plastic strain levels.

3. Constitutive modeling

To model the material behavior in FE simulations, the experiments described in Section 2 were used to identify parameters for strain hardening (Section 3.1) and martensitic transformation kinetics models (Section 3.2). Swift isotropic strain hardening models for the constituent phases in the material were implemented. A two-step approach was taken to model the martensitic transformation at select points of the truncated square pyramid geometry. First, in the full model explicit simulation, for simplicity and to reduce computational expense, the martensitic transformation of each element was neglected. Next, one element implicit simulations from selected locations, corresponding to the measurement locations from experiments, were completed using the combined Swift strain hardening and isotropic martensitic transformation kinetics models [48].

3.1 Swift isotropic strain hardening model for constituent phases

To describe the stress-strain behavior of SS304 with varying α'-martensite volume fraction during deformation, a combined Swift strain hardening law (Eq. 3) for individual phases, i.e., γ-austenite and α'-martensite, was adopted:

$$\bar{\sigma} = f_{\alpha'} \cdot \sigma_{\alpha'} + (1 - f_{\alpha'}) \cdot \sigma_{\gamma}, \tag{3}$$

where:

$$\sigma_{\alpha'} = 1547 \cdot (0.050 + \bar{\varepsilon})^{0.11} \text{ (MPa)} \tag{4}$$

and

$$\sigma_{\gamma} = 1313 \cdot (0.008 + \bar{\varepsilon})^{0.36} \text{ (MPa)}. \tag{5}$$

The weighting factor was based on the α'-martensite volume fraction, $f_{\alpha'}$, and by default, the austenite volume fraction was the remaining portion, i.e., $f_{\gamma} = 1 - f_{\alpha'}$. A similar approach to modeling the equivalent stress for a dual-phase microstructure was used in [61]. The identified stress-strain curve for α'-martensite shows higher flow stress (in the strain range of interest in Figure 4) and a lower hardening rate compared to γ-austenite, consistent with findings in [62,63].

To model the constituent phases, first, uniaxial tension experiments for two materials, SS316L and SS304, were conducted. SS316L experiences minimal deformation induced martensite transformation [64], even with the use of a temperature regulation system to decrease the specimen temperature to 0°C during experiments [65], and remains almost fully austenitic at room temperature. Thus, the stress-strain curve resulting from a SS316L uniaxial test conducted at room temperature (testing procedure is detailed in [66]) and oriented along the RD was assumed to be representative of the stress-strain curve of the austenitic phase (Eq. 5, red curve in Figure 4). Next, the stress-strain curve of the martensitic phase (Eq. 4, blue curve in Figure 4) was determined inversely to fit the α'-martensite volume fraction (green circles in Figure 4) and the stress-strain curve of the SS304 experiment in the RD (black circles in Figure 4). Note that interrupted SS304 uniaxial tension tests were necessary to obtain the α'-martensite volume fraction at several plastic strain levels, and additional information regarding the transformation kinetics model are provided in the next section. Overall, the model shows reasonable agreement with a maximum deviation of 68 MPa from the experimental curve.

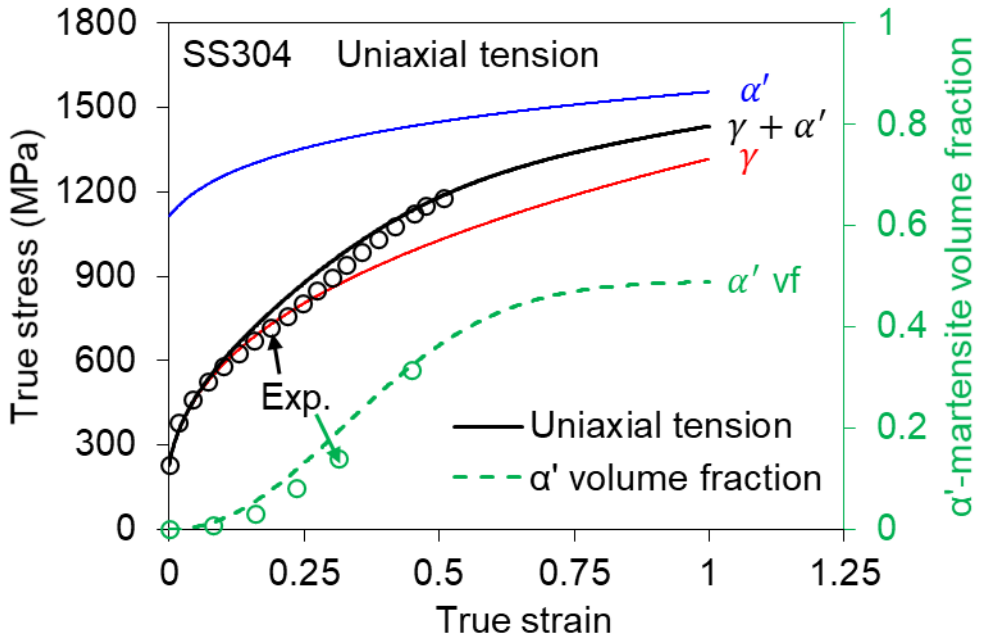

Figure 4. True stress-strain curves for SS304 uniaxial tension experiments, extrapolated Swift model curves for austenite, martensite, and combined material, and α'-martensite volume fraction (right y-axis) from interrupted uniaxial tension experiments and prediction.

3.2 Martensitic transformation kinetics

To model the deformation induced martensite transformation from face centered cubic (FCC) γ -austenite to body centered cubic (BCC) α' -martensite, an isotropic, phenomenological martensitic transformation kinetics model was chosen [48]. This model is based on the rate form of an evolution law proposed by Santacreu et al. [67], which assumes isothermal conditions:

$$\dot{c} = (c_{\max} - c) n D (D\bar{\varepsilon})^{n-1} \dot{\bar{\varepsilon}}, \tag{6}$$

where $\dot{c}$ is the martensitic transformation rate, $c_{\max}$ is the maximum achievable martensite volume fraction for the material at a given temperature, D and n are material parameters, and $\dot{\bar{\varepsilon}}$ is the strain rate. Beese and Mohr [48] expanded this model to include stress state dependency:

$$D = D(\eta, \bar{\theta}) = (D_0 + a_\theta \bar{\theta} + a_\eta \eta)_+, \tag{7}$$

where D_0 is a constant, a_η and a_θ are the contributions of the stress triaxiality, η, and Lode angle parameter, $\bar{\theta}$, to the martensite transformation. Restrictions were included in the model such that $a_\eta \geq 0$ and $a_\theta \geq 0$, and the maximum operator is used so that $D \geq 0$. The stress triaxiality and Lode angle parameter values for each of the four experiments in Section 2, i.e., uniaxial tension, bulge test for equibiaxial tension, in-plane torsion for shear, and uniaxial compression, were calculated assuming isotropic plasticity and are given in Figure 5. The parameters identified for the martensitic transformation kinetics model are listed in Table 2.

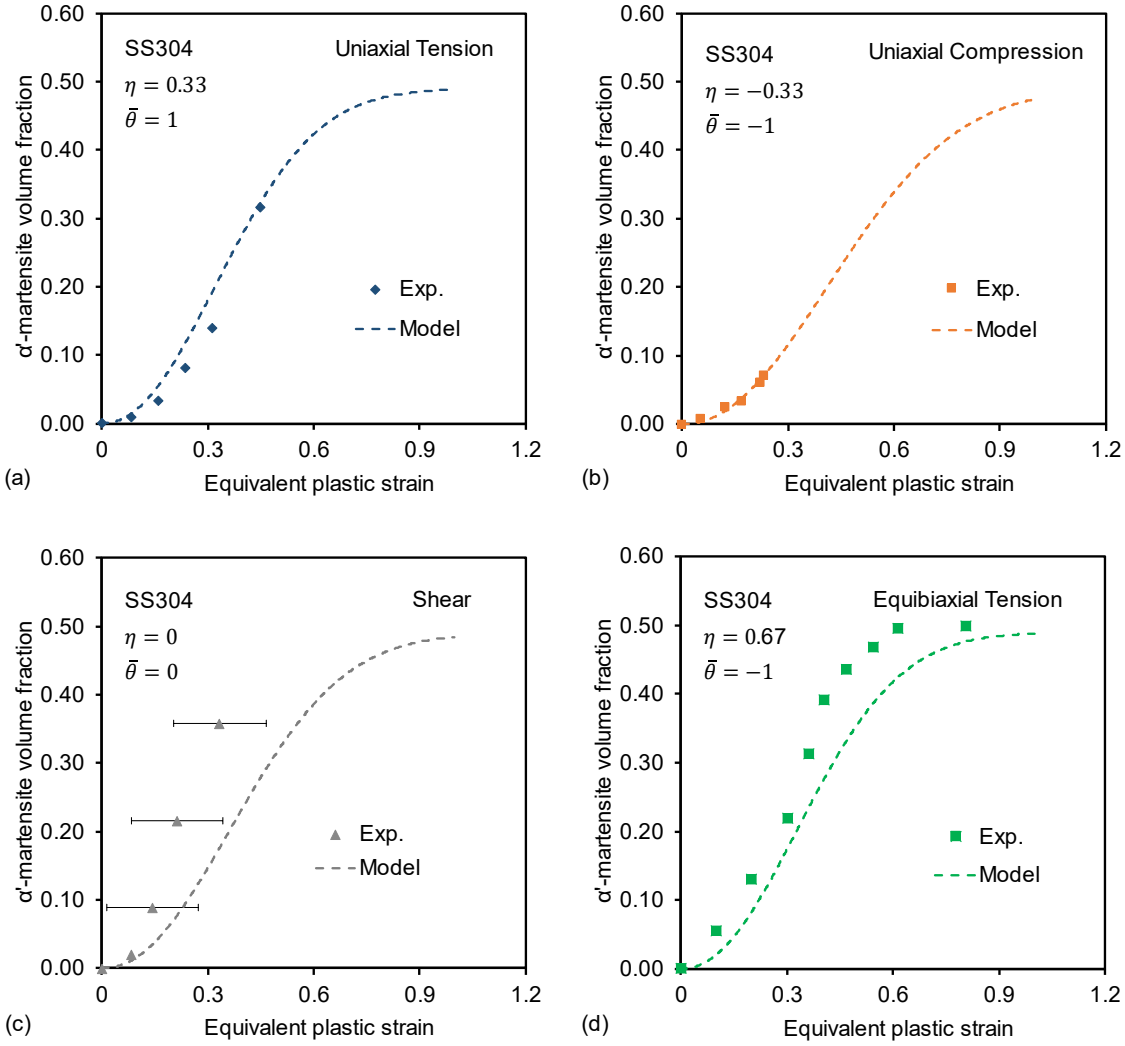

Figure 5. α'-martensite transformation of SS304: experiment and parameter identification for a) uniaxial tension, b) uniaxial compression, c) shear, and d) equibiaxial tension stress states.

Table 2. Parameters for martensitic transformation kinetics model.

$c_{\max}$	n	D_0	a_θ	a_η
0.490	2.129	2.050	0.100	0.463

For the material used in this work, SS304, the order of the curves for each stress state, in Figure 5 from highest to lowest α'-martensite transformation rate with respect to equivalent plastic strain, differs from the trend in other works, e.g., for SS301LN [48], TRIP780 [68], and additively manufactured SS304L [69]. Explicitly, for the SS304 sheet in this study, the martensitic transformation kinetics with respect to equivalent plastic strain from greatest to least are shear, equibiaxial tension, uniaxial tension, and uniaxial compression stress states (Figure 5). For example, at approximately 0.2 equivalent plastic strain, the α'-martensite volume fractions from experiments are 0.216 for shear, 0.130 for equibiaxial tension, 0.081 for uniaxial tension, and 0.060 for uniaxial compression. For the in-plane torsion experiments, the DIC revealed a strong strain gradient, i.e., 0.26 equivalent plastic strain, in the radial direction over a small area of the specimen. Since the Feritscope is only capable of volumetric measurements with an ~3 mm radius, the volume fraction could not be measured precisely for shear, which is denoted by the horizontal error bars with respect to equivalent plastic strain in Figure 5c. The model with the identified parameters for SS304 fits the experimental data for uniaxial tension, uniaxial compression, and equibiaxial tension well.

4. Incremental forming of truncated pyramid

4.1 SPIF experiments

A 5-axis DMU 50 milling machine (DMG Mori) was used to conduct the incremental forming experiments by following a user-specified CNC toolpath, i.e., G-code. A custom frame was mounted inside of the milling machine to clamp the sheet metal blank during forming. The frame contains two hydraulic cylinders that were minimally pressurized to

prevent displacement during the SPIF process. For all experiments, the RD and TD of material orientation were aligned with the x- and y-axis. Figure 6 shows the experimental setup for SPIF.

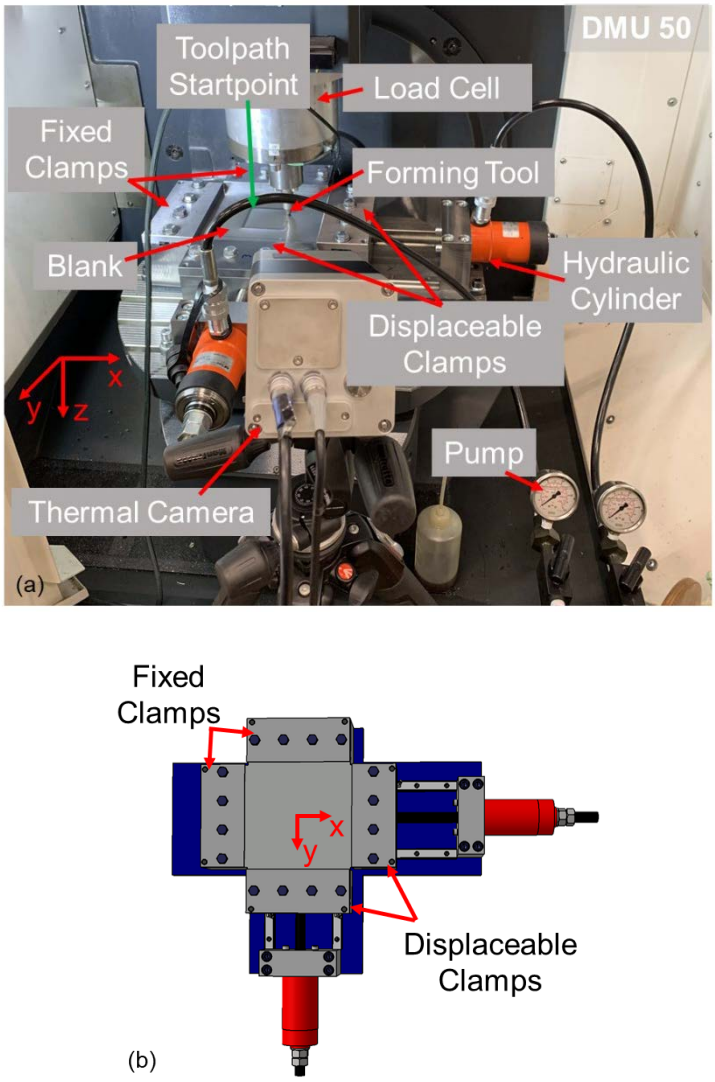

Figure 6. SPIF experimental setup: (a) using DMU 50 machine and (b) schematic of custom frame.

In all incremental forming experiments, a 10 mm diameter hemispherical tool was used with a step down of 0.3 mm. The tool rotation was fixed, i.e., prevented from rotating by setting the rotational speed to 0 rpm, and the feed rate was constant at 1500 mm/min. The toolpath was bidirectional with the start point for each layer located at the location indicated in Figure 6a. An outside-in strategy was used in the toolpath design so that the pyramid was formed from its base to its truncated surface. A deep-drawing oil (Castrol Iloform PN 226 [70]) was evenly applied in a thin layer to the tool contact areas of the blank prior to forming. The total process time to form the truncated pyramid using these parameters was approximately 811 s.

The blanks were laser cut from the 0.8 mm thick sheets of SS304 (EN 1.4307) to create the geometry shown in Figure 7a. Prior to experiments, a square dot pattern with circles that are 1 mm in diameter and spaced 2 mm apart was electrochemically etched onto the side of the blank that would not be contacted by the tool, i.e., non-toolside, for the geometry and surface strain measurements of the deformed part using a 3D optical system after forming. The target geometry was a truncated square pyramid with the dimensions shown in Figure 7b, where β is the wall angle.

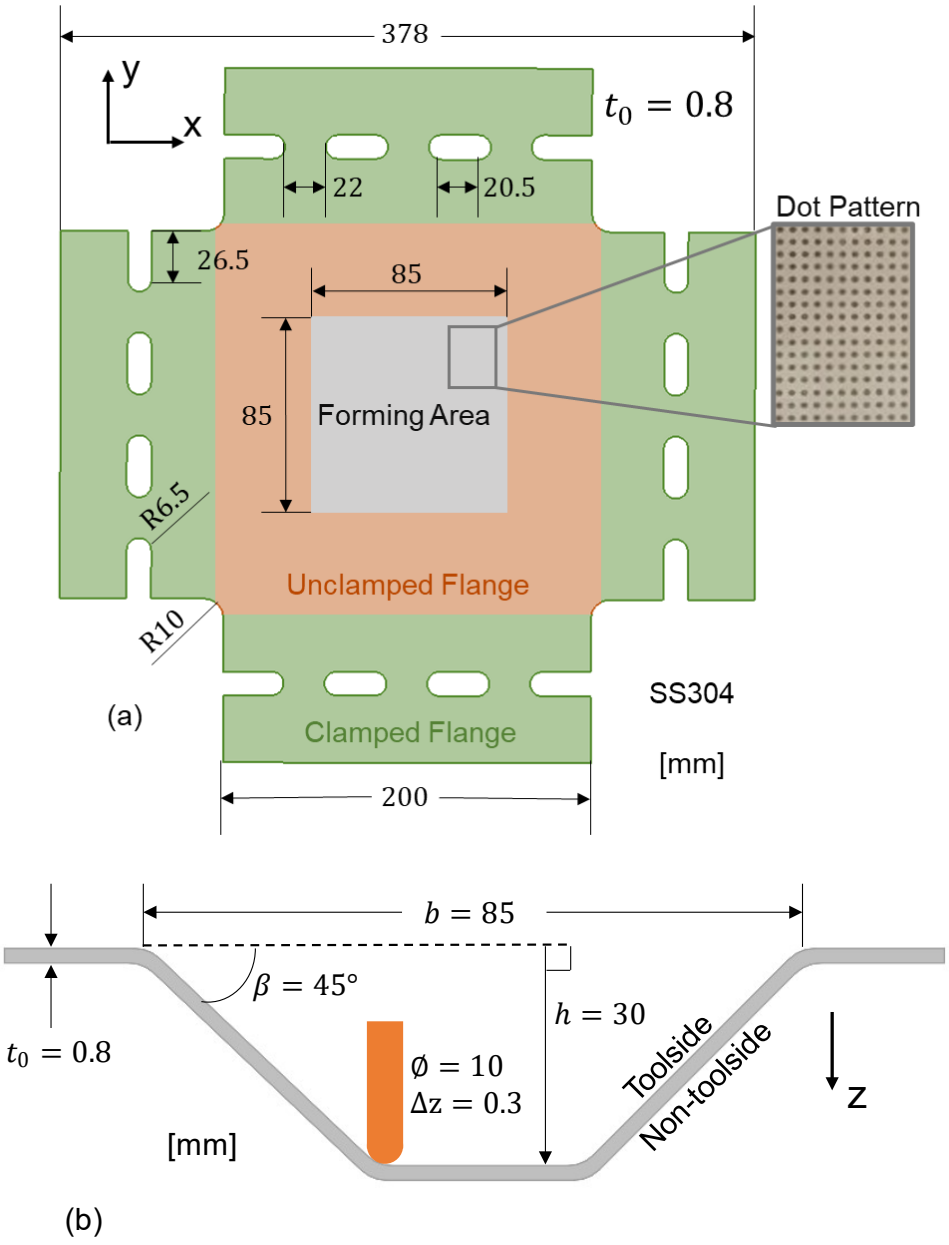

Figure 7. Incremental forming (a) blank and (b) truncated square pyramid geometry.

4.2 Two-step FE simulation

A two-step approach was taken for the numerical analyses of the SPIF process and martensite transformation for SS304 truncated square pyramids. The material models

described in Section 3 were implemented in Abaqus 2019 [71] into a user material subroutine (UMAT) code. First, an explicit model (Section 4.2.1) for SPIF using only the isotropic strain hardening of SS304 was simulated and compared to experimental results. Second, one element implicit models (Section 4.2.2) at locations of interest were completed using the nodal displacement boundary conditions extracted from the full model and a UMAT for the isotropic strain hardening of constituent phases and the martensitic transformation kinetics models. This two-step FE analysis method maximizes computational efficiency, which is a common concern in incremental forming simulations, while providing sufficient analysis of the martensite transformation in SPIF.

4.2.1 Full model simulation for SPIF process

The Abaqus FE model for SPIF is described in [72]. The meshing strategy for the blank was to refine the forming zone (~100 mm x 100 mm), which is slightly larger than the target geometry, and leave the remaining area, i.e., the flange, coarse to reduce the computational expense (Figure 8). Three elements were utilized through the thickness direction of the sheet. The G-code toolpath used in the experiments was entered as amplitudes for displacement boundary conditions in the simulations applied to a rigid tool, i.e., neglecting tool deflection [73]. An implicit step was added to the model to analyze the springback after removing the formed part from the hydraulic frame. Three points on the truncated face of the formed pyramid were selected to fix the displacement during the springback step [74]. Due to the presence of lubrication, friction was neglected in the model. The model parameters used in this work are summarized in Table 3.

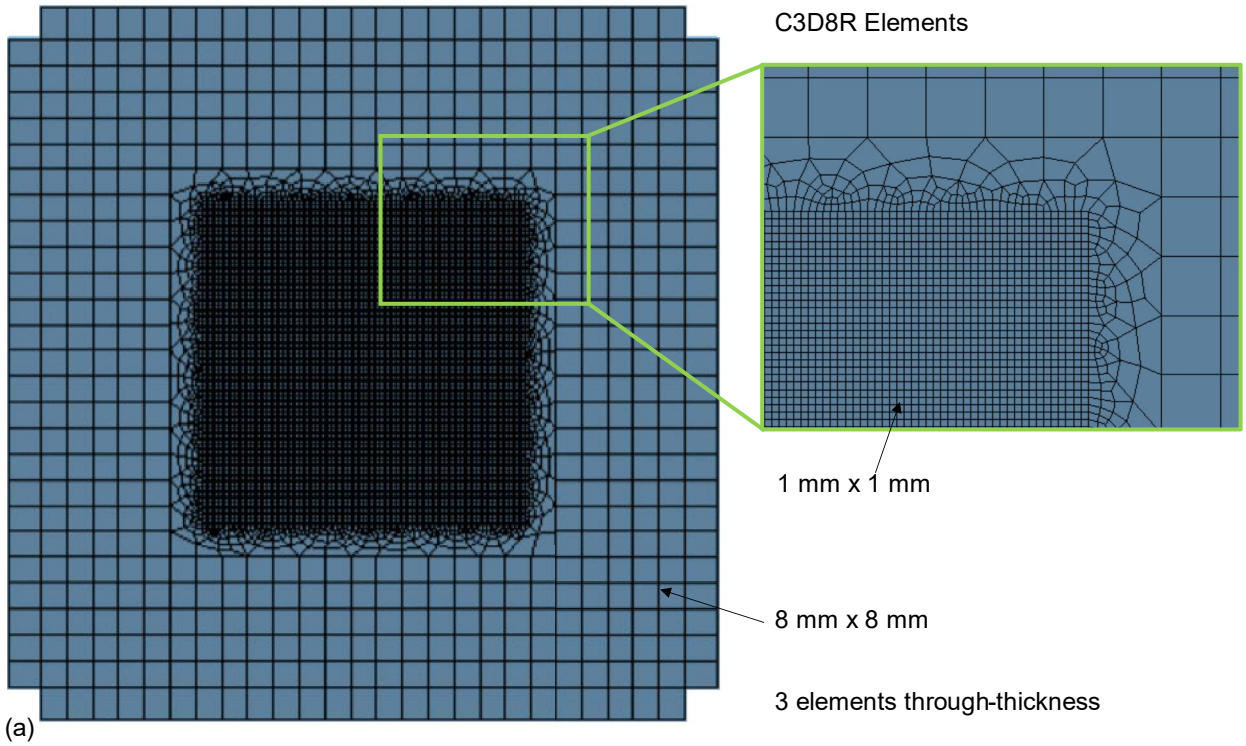

Figure 8. Incremental forming simulations: (a) blank mesh and (b) schematic of two-step FE analysis method with highlighted elements at locations 1-4.

Table 3. Summary of incremental forming full model numerical parameters.

Element type	C3D8R
Number of elements	35180
In-plane element size in refined mesh area	1 mm x 1 mm
In-plane element size in coarse outer area	8 mm x 8 mm
Number of elements through the thickness	3
Mass scaling	10000
Time scaling	1

4.2.2 One element simulation for martensite transformation prediction

A one element implicit FE model was created to investigate the martensite transformation at selected locations corresponding to the Feritscope measurement positions along the wall (Figure 8b). Four elements from the full SPIF model were selected on the toolside, midplane, and non-toolside, i.e., 12 elements in total, along one wall of the truncated square pyramid geometry, and their corresponding nodal displacements, extracted from the full SPIF simulation, were used as the boundary conditions for the one element models. The UMAT, incorporating the martensitic transformation kinetics model coupled with the isotropic strain hardening of constituent phases, was used in the one element simulations to account for the deformation induced phase transformation during the SPIF process.

5. Results and discussion

5.1 Profile of deformed truncated pyramid

To evaluate the geometrical accuracy of the formed part, the cross-sectional profiles along the center lines of the truncated square pyramid were determined in ARGUS (GOM Metrology) and plotted (shown in red) with the target geometry (shown in gray) and FE

predictions (shown in blue) in Figure 9. As denoted in the figure, the solid red line represents the experimental profile measured along the x-direction, and the dashed red line is the experimental profile along the y-direction. The solid blue line is the FE simulation before the springback step, and the dotted blue line is the FE simulation afterward. The truncated face was designated as the reference, i.e., alignment, for the profiles. Experimental geometries were measured after unclamping the formed part with the flange, still included in the part geometry, i.e., after springback. Toolpath optimization using advanced plasticity model capturing Bauschinger effect [75–79] is possible to increase the geometrical accuracy [80] but was not the focus of this work.

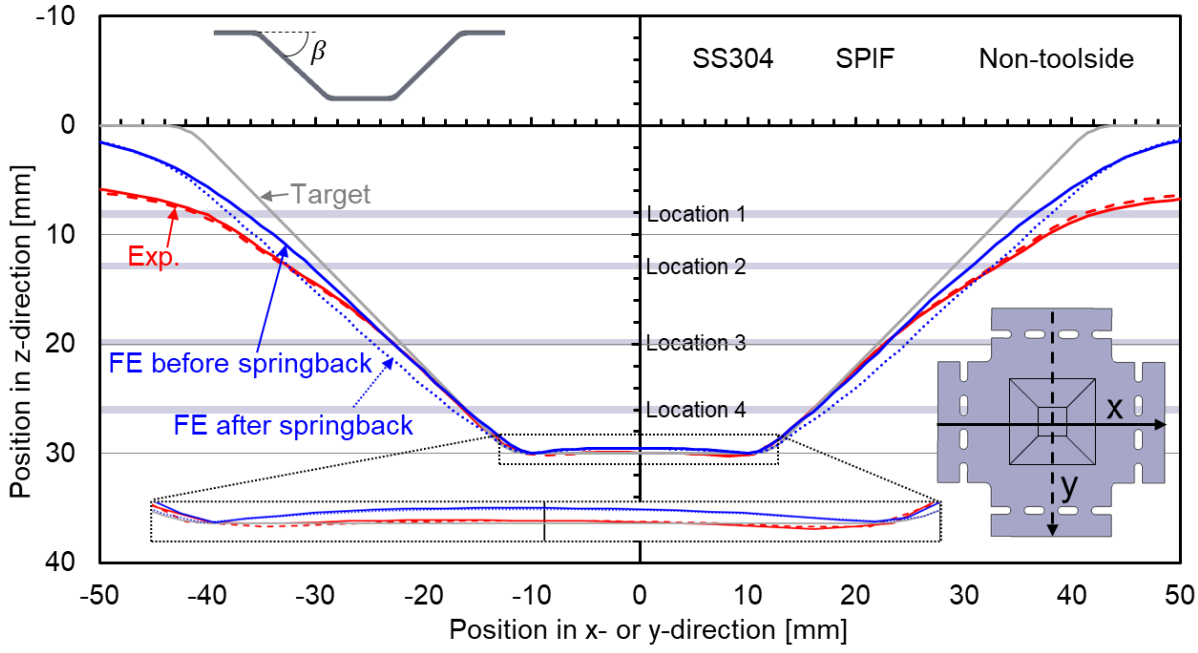

Figure 9. Profile geometry extracted from ARGUS (Exp.) along RD and TD and simulation (FE) before and after springback on non-toolside.

The residual stresses in the part that accumulated during forming directly influence the amount of springback and geometrical accuracy of the final part. The FE simulation and experimental geometries match the target geometry well near the truncated section of the pyramid. However, along the pyramid walls, significant springback caused deviations from the target geometry and decreased the part height (z-dimension). Overall, the FE model prediction was closer to the target geometry, i.e., predicted less springback, particularly comparing the z-dimensions and wall angles, β. At locations 1 and 2, the FE simulation predicted higher geometrical accuracy than observed in the experiments, which is due to the tool deflection that occurred in experiments but was neglected in the FE model. The FE model also predicted a slightly stronger “pillow effect”, i.e., concavity on the truncated face of the pyramid (see Figure 9 inset), than measured in the experiments. This difference of approximately 0.4 mm may be caused by the hardening exponent of the blank material [81]; exclusion of martensitic transformation kinetics in the constitutive model [82]; or ignoring the temperature increase during forming (see Appendix Figure A1).

5.2 Deformation induced martensite transformation

Following SPIF experiments, the α’-martensite volume fraction was measured using an FMP30 Feritscope (Fischer Technology Inc.). On the toolside and non-toolside of the truncated square pyramid part, the α’-martensite volume fraction was probed at four locations along each pyramid wall (Figure 8b). Each measurement was repeated 3-5 times and averaged, with good consistency obtained between the values, +/- 0.036 (maximum). EBSD scans were conducted on a sample extracted at location 3 for validation of the Feritscope measurements (Section 5.2.1).

Figure 10 shows the α'-martensite volume fraction measurements using the Feritscope at four locations along each of the four walls of the truncated square pyramid geometry. At location 1, i.e., near the base of the truncated square pyramid, the α'-martensite volume fraction is the lowest. At locations 2 and 3, the martensite transformation increased, but at location 4, the martensite transformation decreased slightly compared to location 3. The varying α'-martensite volume fraction along the wall is the result of competition between the amount of deformation (shown later in Figures 13 and 14 in Section 5.3), stress states (shown later in Figure 13 in Section 5.3), and the temperature increase during forming (Appendix Figure A1). For locations 1-3, the amount of deformation, i.e., equivalent plastic strain, was the dominating effect, which led to increased transformation at each subsequent location. However, between locations 3 and 4, the accumulated temperature of the part, inhibited the transformation and led to the slight decrease, i.e., <0.01, in α'-martensite volume fraction shown in Figure 10 at location 4. Experimentally, the maximum recorded temperature at location 3 was approximately 60°C (see Figure A1), and the part temperature increased during forming to approximately 68°C when the tool was located near location 4. Additionally, the equivalent plastic strain level for the element on the toolside was slightly decreased at location 4 compared to location 3 by approximately 0.04, which could be a minor effect on the lower α'-martensite volume fraction. The α'-martensite volume fraction measurements on the non-toolside were consistently lower than the toolside (by ~10%) but show the same trend (Figure 10). This is consistent with the increased equivalent plastic strain (shown later in Figure 14 in Section 5.3) on the toolside during SPIF, which is caused by the tool contacting the sheet and creating localized shear strain as the main

strain component [83]. The differences in the measurements for the four sides of the pyramids are potentially due to the bidirectional toolpath, i.e., the positive x-y corner where the step-down to the next toolpath layer switched directions, alternating between clockwise and counterclockwise.

To validate the apparent martensite transformation gradient revealed by the Feritscope measurements, EBSD analyses were conducted in the plane of the sheet near the surface of location 3 of the pyramid wall. As shown in Figure 10, the EBSD α'-martensite measurements were consistently ~0.06 greater than the Feritscope measurements, which may be caused by the fact that EBSD measures a highly localized area at the surface in comparison to the volumetric measurements of the Feritscope. In addition, the sample preparation, i.e., grinding and polishing, required for EBSD may increase the α'-martensite transformation locally [84]. The scanning electron microscope (SEM) and EBSD parameters used for these analyses are shown in Table 4.

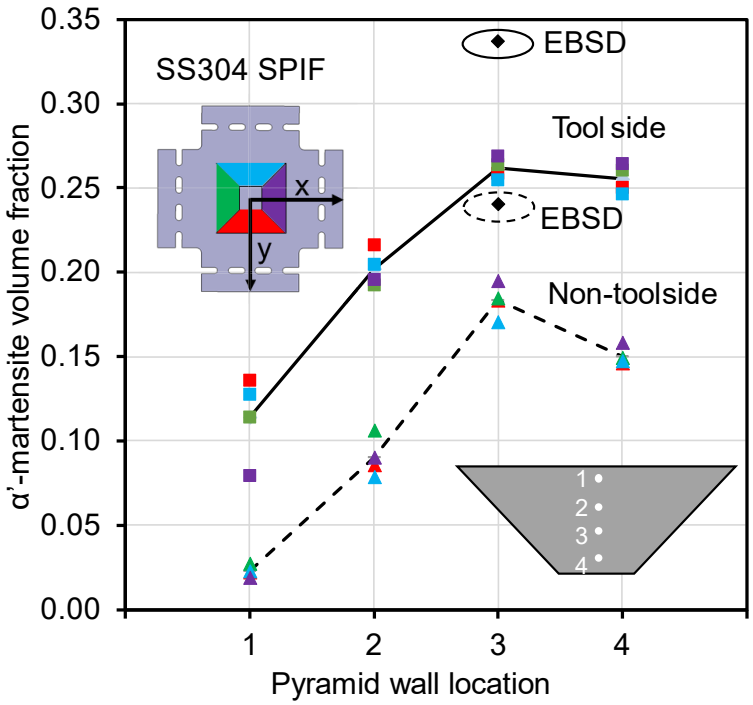

Figure 10. α'-martensite volume fraction measured by Feritscope at four locations along each pyramid wall on toolside (squares) and non-toolside (triangles). Colors indicate pyramid walls. Average of four sides at each location for tool (solid) and non-tool (dashed) sides are shown as lines. EBSD measurements at location 3 (diamonds) are circled.

Table 4. SEM and EBSD parameters for phase identification.

Magnification (x)	750
Beam Intensity	19.1
Acceleration Voltage (kV)	10
Sample Tilt (°)	70
Binning	8x8
Step Size (μm)	0.7

In addition, an EBSD sample was prepared and analyzed along the thickness direction, i.e., RD-ND plane, at location 3 to further validate the Feritscope measurement. At the designated magnification, two to three scans were needed to cover the entire thickness direction. The results were then merged for each sample and divided into three sections for the SPIF sample as shown in Figure 11. The same trend apparent in the Feritscope measurements, i.e., the toolside measurements are greater than the non-toolside measurements, was observed in these EBSD results. A significant α'-martensite layer is visible on the toolside, which agrees with the increased strain observed on the toolside of the finite element simulations and contributes to the martensite transformation gradient. A similar increase in the α'-martensite volume fraction was observed when preparing the as-received material sample for EBSD (Figure 11).

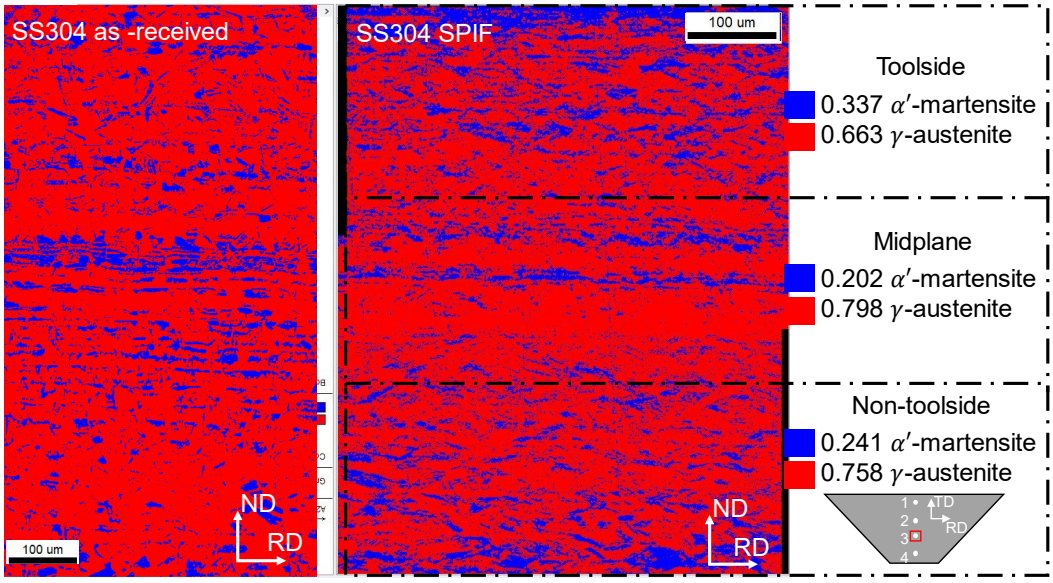

Figure 11. Volume fraction measurements obtained by EBSD along thickness direction: (a) as-received material and (b) location 3 of SPIF truncated square pyramid sample.

Near the midplane, elongated bands of α'-martensite were observed in both EBSD scans, which have also been revealed in microscopy of TRIP steels by researchers at the National Institute of Standards and Technology (NIST) and elsewhere [85]. One possible explanation is that the rolling process used to manufacture the sheet to the as-received thickness creates a complex stress profile through the thickness. Thus, the resulting material composition may not be homogeneous [86]. Consequently, the material at varying layers along the thickness direction has different levels of susceptibility to martensite transformation with additional deformation. Specifically, from Figure 11, the polishing procedure used for SS304 resulted in increased martensite transformation in the form of α'-martensite bands near the midplane since the bands are visible in both the as-received and SPIF samples.

Results from the two-step FE simulations are shown in Figure 12 along with the experimental results for comparison. In addition to the toolside and non-toolside, the FE model also offered predictions for the midplane of the specimen, which was not possible to isolate and measure using the Feritscope. The midplane values fell between the toolside and non-toolside values, which is different from the through-thickness gradient observed by EBSD (shown for location 3 in Figure 11). To predict this gradient more accurately, additional elements could be added in the thickness direction in the numerical model at increased computational cost.

Overall, the experiments and FE predictions showed good agreement for both the toolside and non-toolside. Half of the differences between the Feritscope and FE predictions were within the range of the variation measured between the four faces of the pyramids from experiments (Figure 10). The largest difference was observed at location

1 on the toolside. Due to the sigmoidal relationship between α'-martensite volume fraction and equivalent plastic strain, at small plastic strain levels, e.g., near location 1, larger error with respect to martensite transformation was possible. Again, note that the simulation neglected tool deflection, and the accuracy of the martensitic transformation kinetics model with respect to shear was not achieved due to the limitations of the Feritscope in this study.

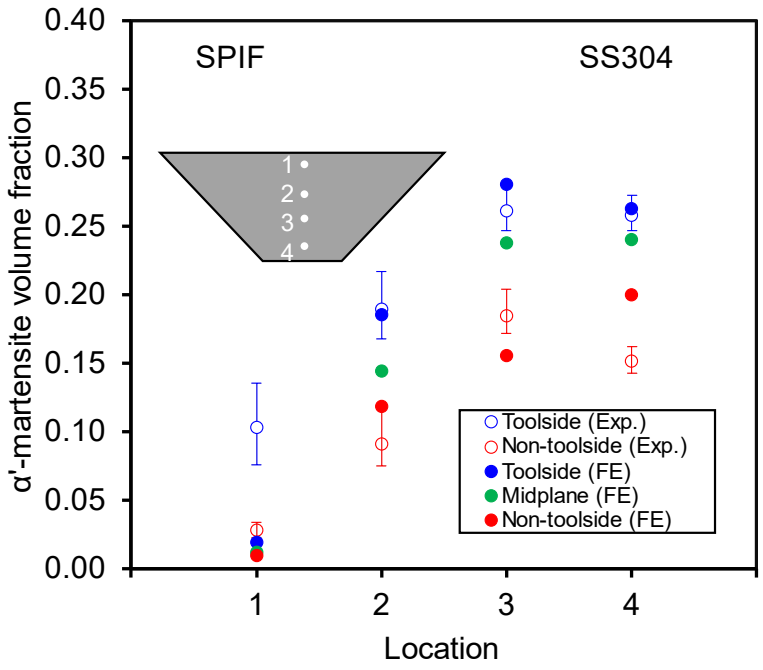

Figure 12. Comparison of α'-martensite volume fraction measurements from Feritscope (Exp.) and predictions from simulations (FE) using the martensite transformation kinetics model.

5.3 Stress state and strain evolution during deformation

To further investigate the effect of the martensitic transformation, the stress state evolution during SPIF was analyzed from the FE simulations. The stress triaxiality and

Lode angle parameter, which are the parameters of martensite transformation kinetics model, on the toolside and non-toolside at locations 1-4, are shown in Figure 13. Only the stress states corresponding to an equivalent plastic strain increase, i.e., $\Delta\bar{\varepsilon}$, > 0.001 were plotted in this figure. This equivalent plastic strain threshold excludes stress state changes when the tool was sufficiently far away from the locations of interest so did not directly impact the plastic deformation and martensite transformation at these points. The stress triaxiality varied with respect to both time and location. The colored bands in Figure 13 correspond to the final equivalent plastic strain values for elements at locations 1-4, where data points were concentrated in the unfiltered data set (Appendix Figure A2).

Locations 1, 2, and 4 on the toolside had positive stress triaxialities, indicating plane strain tension (red, green, and purple symbols in Figure 13a) throughout the forming process. Location 3 on the toolside trended from positive to negative stress triaxialities, i.e., from plane strain tension to shear to plane strain compression (in correlation with the Lode angle parameter), as the forming progressed (blue symbols in Figure 13a).

Due to the large number of factors affecting the martensitic transformation, it is challenging to isolate their individual contributions. From Figure 12, location 3 underwent the largest martensitic transformation out of the four pyramid wall locations. The evolution of the stress state through shear, i.e., the stress state with the highest martensitic transformation kinetics of the investigated material (Figure 5), is a possible reason for the increased volume fraction at location 3 as predicted in the FE simulation. Note that the difference of equivalent plastic strain at locations 3 and 4 is very small to cause the lower martensite transformation at location 4, and the temperature effect is excluded in the FE model. This indicates that the highest martensite volume fraction at location 3 should be

related to the stress state during the process as well as the accumulated deformation and temperature effects.

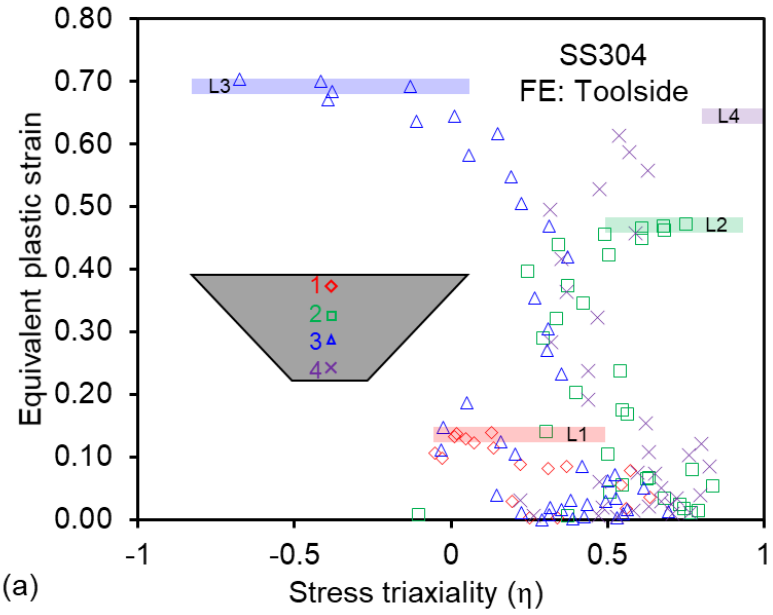

(a)

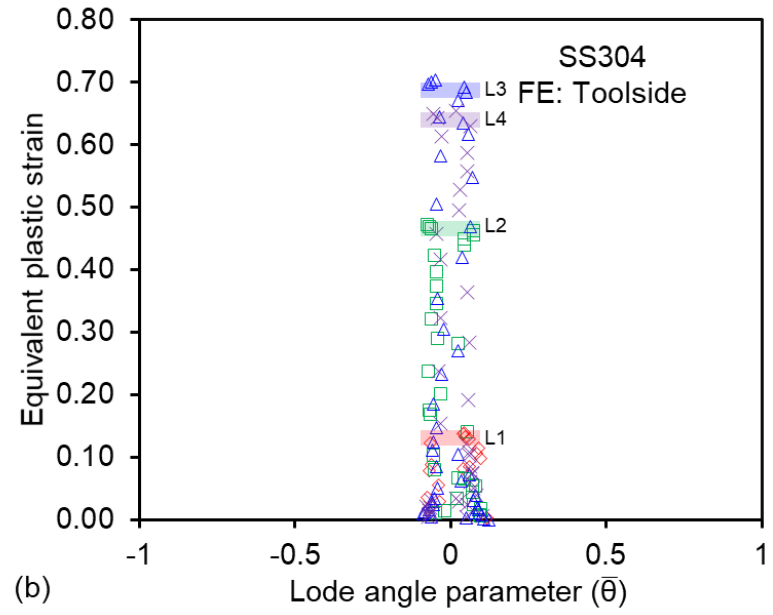

(b)

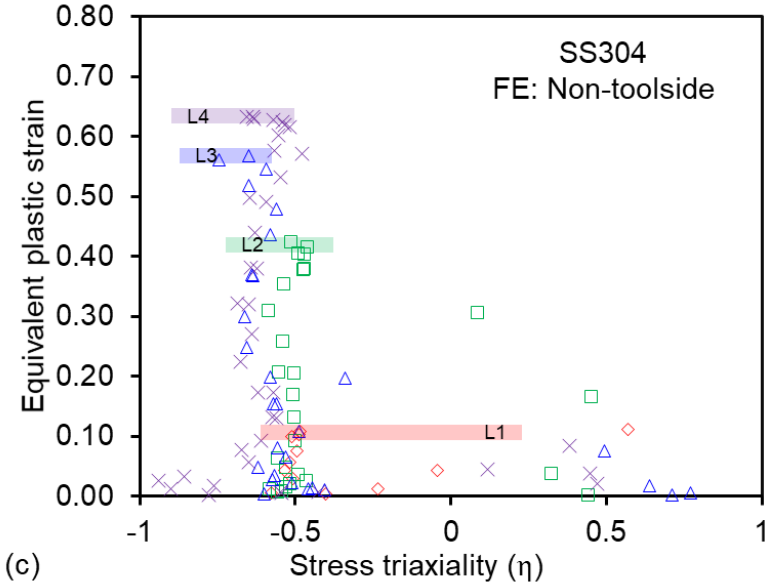

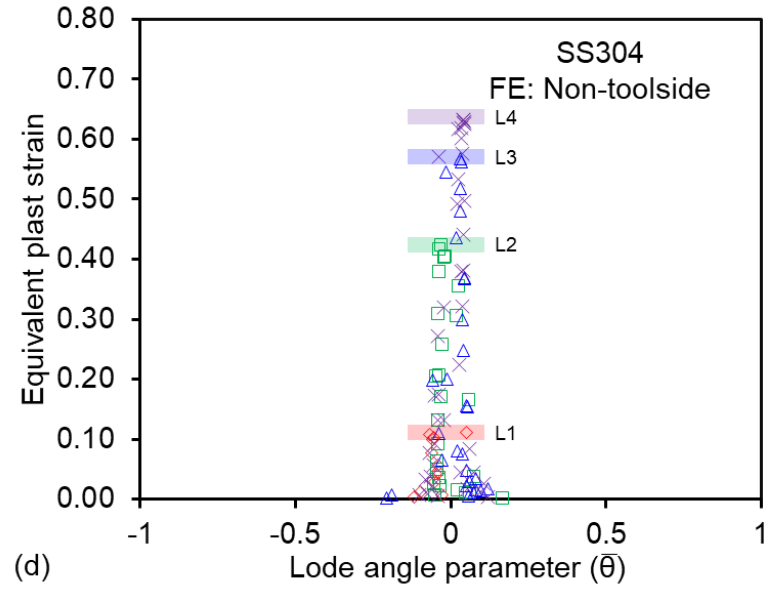

Figure 13. Stress state evolution from FE simulations ($\Delta\bar{\varepsilon} > 0.001$): toolside (a) stress triaxiality and (b) Lode angle parameter; non-toolside (c) stress triaxiality and (d) Lode angle parameter at locations 1-4. Bars indicate the equivalent plastic strain saturation at each location.

On the non-toolside, the stress triaxiality oscillates for the four locations around plane strain compression based on the location of the tool and its proximity to the elements of interest. A negative stress triaxiality value for the toolside and a positive stress triaxiality value for the non-toolside were recorded when the tool was located directly at the element of interest. For both the toolside and non-toolside, the evolution of the stress triaxiality, i.e., variation with respect to the x-axis in Figure 13, was significantly higher than that of the Lode angle parameter. Thus, for this material and part geometry during SPIF, stress triaxiality had a larger influence on the martensite transformation than Lode angle parameter. This is in agreement with the martensitic transformation kinetics model parameters identified in this work for SS304, where $a_\eta > a_\theta$.

In addition to the evolution of the stress states, the equivalent plastic strain contours for the toolside and non-toolside are shown in Figure 14. The equivalent plastic strain was larger on the toolside, particularly on the faces of the pyramid walls and near the lateral edges, which is in agreement with Jackson and Allwood [83]. Their work also showed that the tool contact increases the shear strains on the toolside compared to the non-toolside. These equivalent plastic strain trends for the toolside and non-toolside support the martensitic transformation predictions and trends shown in Figure 12.

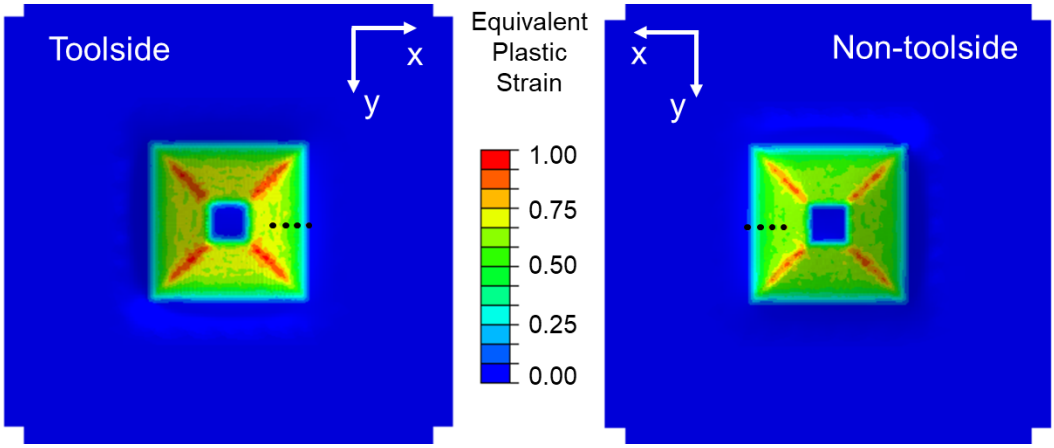

Figure 14. Equivalent plastic strain from SPIF FE simulations on toolside and non-toolside of truncated square pyramid. Black dots represent locations 1 through 4.

6. Conclusions and Outlook

SPIF was used to manufacture truncated square pyramids from SS304. The α'-martensite volume fraction was measured using a Feritscope and validated by EBSD. SS304 was characterized by experiments for four stress states and used to construct a material model for FE analyses. Swift isotropic hardening for each phase and a martensitic transformation kinetics model with all parameters identified from experimental data were implemented in a UMAT subroutine code. A two-step FE analysis was implemented to predict the martensite transformation and showed good agreement with experimental results. Additionally, the FE analyses provided valuable insight into the increased deformation on the toolside compared to the non-toolside for SPIF and the martensitic transformation at the midplane, which was not directly measurable using the Feritscope. Analyzing the stress states during SPIF from the simulations also revealed that the stress triaxiality had a larger effect on the martensite transformation than the Lode angle parameter for this particular material and geometry. The stress state variation, deformation, and temperature effects contributed to the variance of martensite transformation in the formed components.

The results support that SPIF can be used to create functionally graded materials. The martensite transformation in the truncated square pyramid components varied through the sheet thickness and along the pyramid walls as observed by Feritscope, EBSD, and FE simulations. Standard material characterization experiments with Feritscope measurements at different strain levels were sufficient for identifying parameters for a SS304 material model with strain hardening of each phase and martensitic transformation kinetics. The two-step FE approach to predicting the martensite transformation produced

satisfactory results without requiring significant computational expense. In addition to being replicated for other metal forming processes, this approach to characterize the transformation kinetics could be applied to other materials or to include additional considerations, e.g., temperature. Depending on the desired level of accuracy, a more complex transformation kinetics model, i.e., a model that includes additional parameters, could be used at added computational expense. Control of the stress state, particularly the stress triaxiality, during SPIF through toolpath manipulations will allow targeted material properties to be achieved in the final components based on their intended application.

Acknowledgements

Support for the New Hampshire Center for Multiscale Modeling and Manufacturing of Biomaterials (NH BioMade) project was provided by the US National Science Foundation (NSF) EPSCoR award (#1757371). This research was also supported by the Institute of International Education Graduate International Research Experiences program (NSF #1829436), the German-American Fulbright Commission, and the Germanistic Society of America.

The authors would like to thank Dirk Hoffmann for his assistance with laser cutting specimens and Lucas Bueren, Bastian Hoppe, Lenard Polec, and Oliver Schulz for assistance with material characterization experiments at the IUL. Special thanks also to Dr. Thomas Gnäupel-Herold and Dr. Adam Creuzinger at the National Institute for Standards and Technology (NIST) for insightful discussions regarding the EBSD results.

The authors would also like to thank Nancy Cherim for assistance with the EBSD scans. The SEM/FIB used is managed by the University Instrumentation Center (UIC) at the University of New Hampshire (UNH) and was purchased with funds awarded to UNH from the US National Science Foundation (NSF) (MRI Grant 1337897) with additional funds from UNH. EDS/EBSD components on this system were purchased with start-up funds from UNH at the discretion of Prof. Marko Knezevic.

Appendix

A1. Temperature

The temperature field during the process was measured by an infrared camera (VarioCAM HD head) and analyzed using IRBIS 3 (InfraTec) software. During SPIF, the process temperature increased significantly, ~50°C, while forming the truncated square pyramid part (Figure A1). This temperature increase inhibited the maximum martensitic transformation that occurred. Note that the maximum temperature occurs beneath the forming tool and is not visible to the IR camera, so the actual process temperature was greater than the values shown in Figure A1. Some thermal effects were captured in the numerical model due to the ~20°C increase observed during the uniaxial tension experiment used for material model fitting (Figure 4). However, since the temperature increase during SPIF is greater than in UT, some thermal effects were neglected in the simulation. If desired for future experimentation or industrial implementation, temperature regulation can be added to the process setup to enhance the martensite transformation. For example, vortex tubes can be mounted to the machine's spindle to locally cool the forming area [87].

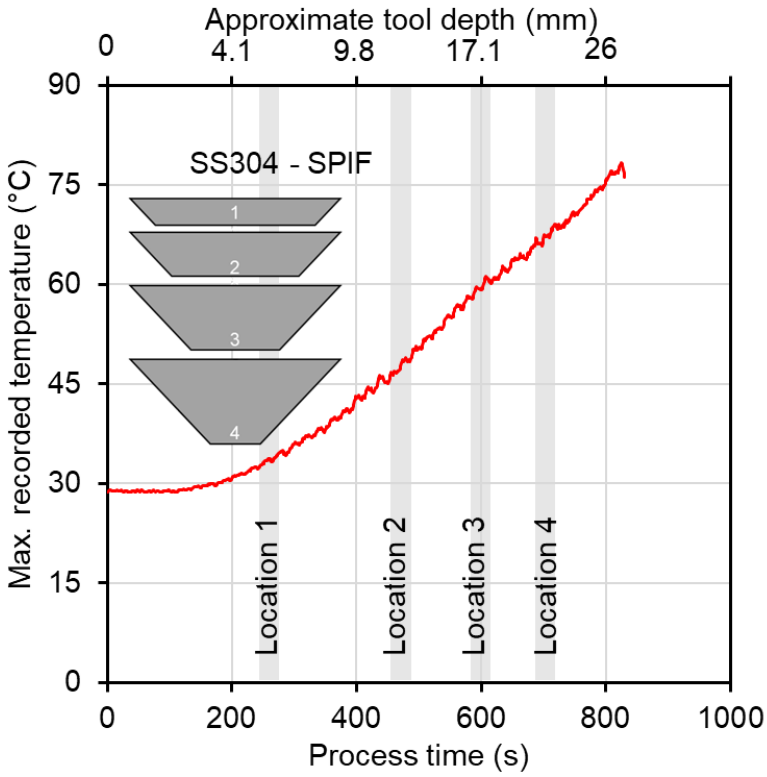

Figure A1. Temperature recorded during SPIF experiments.

A2. Stress triaxiality and Lode angle parameter change

From the FE simulations, the stress triaxiality and Lode angle parameter with respect to equivalent plastic strain extracted from the four locations of interest are shown in Figure A2. The data points tend to saturate at the final equivalent plastic strain level for each location and can be seen as the darker areas in the figure. After filtering the data by the change in plastic equivalent strain as shown in Figure 13, many of these data points are eliminated. Thus, they are replaced by color bars in Figure 13 to clearly mark the final strain level and approximate stress state.

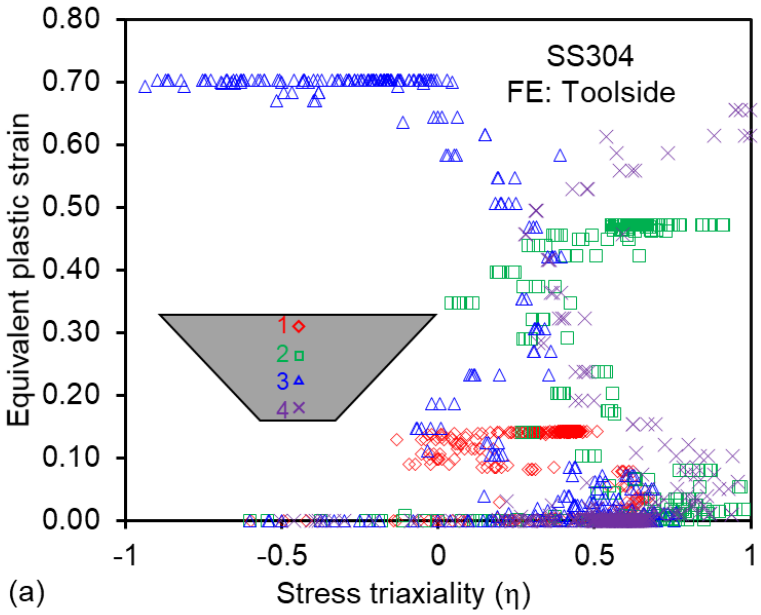
SS304
FE: Toolside
Equivalent plastic strain
0.80
0.70
0.60
0.50
0.40
0.30
0.20
0.10
0.00
1
2
3
4
-1
-0.5
0
0.5
1
Stress triaxiality (η)

(a)

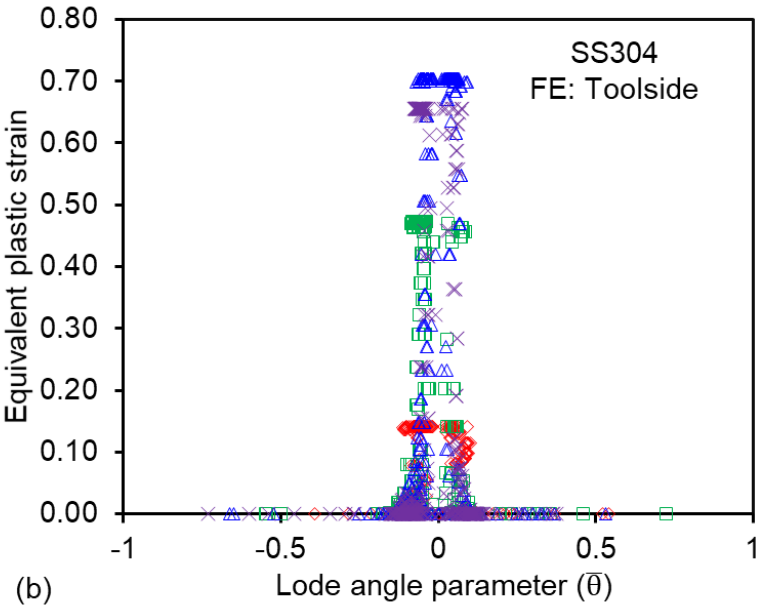
SS304
FE: Toolside
Equivalent plastic strain
0.80
0.70
0.60
0.50
0.40
0.30
0.20
0.10
0.00
-1
-0.5
0
0.5
1
Lode angle parameter (θ̄)

(b)

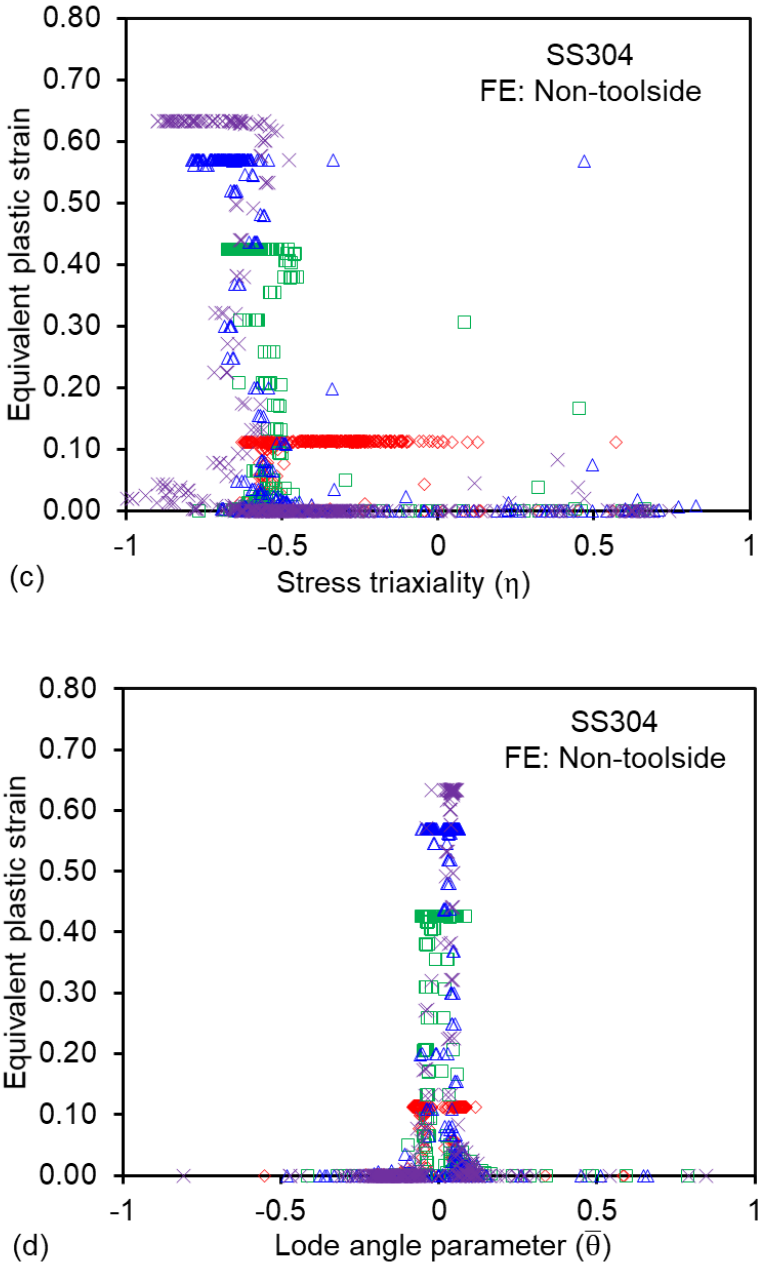

Figure A2. Stress state evolution from FE simulations: toolside (a) stress triaxiality and (b) Lode angle parameter; non-toolside (c) stress triaxiality and (d) Lode angle parameter at locations 1-4.

References

[1] Kalpakjian S, Schmid S. Manufacturing Engineering and Technology. 7th ed. Pearson Education; 2013.

[2] Ceretti E, Giardini C, Attanasio A. Experimental and simulative results in sheet incremental forming on CNC machines. Journal of Materials Processing Technology 2004;152:176–84. https://doi.org/10.1016/j.jmatprotec.2004.03.024.

[3] Schafer T, Schraft RD. Incremental sheet metal forming by industrial robots. Rapid Prototyping Journal 2005;11:278–86. https://doi.org/10.1108/13552540510623585.

[4] Cao J, Huang Y, Reddy NV, Malhotra R, Wang Y. Incremental sheet metal forming: Advances and challenges, 2008, p. 1967–82.

[5] McAnulty T, Jeswiet J, Doolan M. Formability in single point incremental forming: A comparative analysis of the state of the art - ScienceDirect. CIRP Journal of Manufacturing Science and Technology 2017;16:43–54. https://doi.org/10.1016/j.cirpj.2016.07.003.

[6] Roth GA, Geraci CL, Stefaniak A, Murashov V, Howard J. Potential occupational hazards of additive manufacturing. J Occup Environ Hyg 2019;16:321–8. https://doi.org/10.1080/15459624.2019.1591627.

[7] Groche P, Breunig A, Chen K, Molitor DA, Ha J, Kinsey BL, et al. Effectiveness of different closed-loop control strategies for deep drawing on single-acting 3D Servo Presses. CIRP Annals 2022;71:357–60.

[8] Chen K, Breunig A, Ha J, Kinsey BL, Groche P, Korkolis YP. Robustness of deep-drawing finite-element simulations to process variations. Int J Mater Form 2022;15:45. https://doi.org/10.1007/s12289-022-01695-3.

[9] Emmens WC, van den Boogaard AH. Incremental forming by continuous bending under tension—An experimental investigation. Journal of Materials Processing Technology 2009;209:5456–63. https://doi.org/10.1016/j.jmatprotec.2009.04.023.

[10] Ha J, Mayer S, Feng Z, Matukhno N, Knezevic M, Kinsey BL. Inducing <111> texture in AA5182-O through continuous-bending-under-tension and recovery heat treatment processes to influence r-values. CIRP Annals 2022;71:249–52. https://doi.org/10.1016/j.cirp.2022.04.059.

[11] Mamros EM, Polec LA, Maaß F, Clausmeyer T, Tekkaya AE, Ha J, et al. Examination of bending stress superposition effect on martensite transformation in austenitic stainless steel 304, France: 2023.

[12] Allwood JM, Shouler DR, Tekkaya AE. The Increased Forming Limits of Incremental Sheet Forming Processes. Key Engineering Materials 2007;344:621–8. https://doi.org/10.4028/www.scientific.net/KEM.344.621.

[13] Duflou JR, Habraken A-M, Cao J, Malhotra R, Bambach M, Adams D, et al. Single point incremental forming: state-of-the-art and prospects. Int J Mater Form 2018;11:743–73. https://doi.org/10.1007/s12289-017-1387-y.

[14] Tisza M. General overview of sheet incremental forming. Journal of Achievements in Materials and Manufacturing Engineering 2012:113–20.

[15] Edward L. Apparatus and process for incremental dieless forming. US3342051A, 1967.

[16] Hagan E, Jeswiet J. A review of conventional and modern single-point sheet metal forming methods. Proceedings of the Institution of Mechanical Engineers, Part B: Journal of Engineering Manufacture 2003;217:213–25. https://doi.org/10.1243/095440503321148858.

[17] Lu B, Fang Y, Xu DK, Chen J, Ou H, Moser NH, et al. Mechanism investigation of friction-related effects in single point incremental forming using a developed oblique roller-ball tool. International Journal of Machine Tools and Manufacture 2014;85:14–29. https://doi.org/10.1016/j.ijmachtools.2014.04.007.

[18] Grimm TJ, Ragai I, Roth JT. A Novel Modification to the Incremental Forming Process, Part 1: Multi-directional Tooling. Procedia Manufacturing 2017;10:510–9. https://doi.org/10.1016/j.promfg.2017.07.035.
[19] Adams D, Jeswiet J. Single-point incremental forming of 6061-T6 using electrically assisted forming methods. Proceedings of the Institution of Mechanical Engineers, Part B: Journal of Engineering Manufacture 2014;228:757–64. https://doi.org/10.1177/0954405413501670.
[20] Grimm TJ, Ragai I, Roth JT. The Effects of Polarity and Current Path in Electrically Assisted Single Point Incremental Forming of 2024-T3 Aluminum, American Society of Mechanical Engineers Digital Collection; 2017. https://doi.org/10.1115/MSEC2017-3037.
[21] Min J, Seim P, Störkle D, Thyssen L, Kuhlenkötter B. Electrically-assisted Incremental Sheet Forming of Advanced High Strength Steels. Procedia Manufacturing 2017;7:22–6. https://doi.org/10.1016/j.promfg.2016.12.009.
[22] Rodriguez-Alabanda O, Guerrero-Vaca G. Influence of single point incremental forming on the quality and surface properties of parts manufactured with aluminized steel sheets pre-coated with PTFE. CIRP Journal of Manufacturing Science and Technology 2022;38:215–29. https://doi.org/10.1016/j.cirpj.2022.04.014.
[23] Hassan AA, Küçüktürk G, Yazgin HV, Gürün H, Kaya D. Selection of Constitutive Material Model for the Finite Element Simulation of Pressure-Assisted Single-Point Incremental Forming. Machines 2022;10:941. https://doi.org/10.3390/machines10100941.
[24] Maaß F, Hahn M, Dobecki M, Thannhäuser E, Tekkaya AE, Reimers W. Influence of tool path strategies on the residual stress development in single point incremental forming. Procedia Manufacturing 2019;29:53–8. https://doi.org/10.1016/j.promfg.2019.02.105.
[25] Rashid H, Hussain G, Rehman K, Khan S, Alkahtani M, Abidi MH. Characterization of residual stresses in an asymmetrical shape produced through incremental forming. CIRP Journal of Manufacturing Science and Technology 2020;31:478–91. https://doi.org/10.1016/j.cirpj.2020.07.010.
[26] Ruszkiewicz B, Dodds S, Reese Z, Roth J, Ragai I. Incrementally Formed Stiffeners Effect on the Reduction of Springback in 2024-T3 Aluminum After Single Point Incremental Forming. Proceedings of the ASME 2015 International Manufacturing Science and Engineering Conference., vol. 1, Charlotte, North Carolina, USA: ASME; 2015. https://doi.org/10.1115/MSEC2015-9437.
[27] Ndip-Agbor E, Cheng P, Moser N, Ehmann K, Cao J. Prediction of rigid body motion in multi-pass single point incremental forming. Journal of Materials Processing Technology 2019;269:117–27. https://doi.org/10.1016/j.jmatprotec.2019.02.007.
[28] Malhotra R, Cao J, Ren F, Kiridena V, Cedric Xia Z, Reddy NV. Improvement of Geometric Accuracy in Incremental Forming by Using a Squeezing Toolpath Strategy With Two Forming Tools. J Manuf Sci Eng 2011;133. https://doi.org/10.1115/1.4005179.
[29] Gao L, Zhao Y, Yu Z, Yan H. Formability analysis of electrically assisted double-side multi-point incremental sheet forming. Int J Adv Manuf Technol 2020;108:3405–17. https://doi.org/10.1007/s00170-020-05576-4.
[30] Darzi S, Adams MD, Roth JT, Kinsey BL, Ha J. Manipulating Martensite Transformation of SS304L During Double-Sided Incremental Forming by Varying Temperature and Deformation Path. CIRP Annals Manufacturing Technology 2023.
[31] Darzi S, Kinsey BL, Ha J. Reforming toolpath effect on deformation mechanics in double-sided incremental forming. International Journal of Mechanical Sciences 2024:109548.
[32] Maaß F, Hahn M, Tekkaya AE. Interaction of Process Parameters, Forming Mechanisms, and Residual Stresses in Single Point Incremental Forming. Metals 2020;10:656. https://doi.org/10.3390/met10050656.

[33] Maqbool F, Bambach M. Dominant deformation mechanisms in single point incremental forming (SPIF) and their effect on geometrical accuracy. International Journal of Mechanical Sciences 2018;136:279–92. https://doi.org/10.1016/j.ijmecsci.2017.12.053.
[34] Kim YH, Park JJ. Effect of process parameters on formability in incremental forming of sheet metal. Journal of Materials Processing Technology 2002;130–131:42–6. https://doi.org/10.1016/S0924-0136(02)00788-4.
[35] Ha J, Fones J, Kinsey BL, Korkolis YP. Plasticity and Formability of Annealed, Commercially-Pure Aluminum: Experiments and Modeling. Materials 2020;13:4285. https://doi.org/10.3390/ma13194285.
[36] Ha J, Korkolis YP. Hole-Expansion: Sensitivity of Failure Prediction on Plastic Anisotropy Modeling. Journal of Manufacturing and Materials Processing 2021;5:28. https://doi.org/10.3390/jmmp5020028.
[37] Emmens WC, van den Boogaard AH. An overview of stabilizing deformation mechanisms in incremental sheet forming. Journal of Materials Processing Technology 2009;209:3688–95. https://doi.org/10.1016/j.jmatprotec.2008.10.003.
[38] Martínez-Donaire AJ, Borrego M, Morales-Palma D, Centeno G, Vallellano C. Analysis of the influence of stress triaxiality on formability of hole-flanging by single-stage SPIF. International Journal of Mechanical Sciences 2019;151:76–84. https://doi.org/10.1016/j.ijmecsci.2018.11.006.
[39] Lonardelli I, Bosetti P, Bruschi S, Molinari A. On the Formability and Microstructural Characteristics of AISI 301 Parts Formed by Single-Point Incremental Forming. KEM 2011;473:869–74. https://doi.org/10.4028/www.scientific.net/KEM.473.869.
[40] Katajarinne T, Kivivuori S. Strain Induced Martensite in Incremental Forming - Formation, Effect and Control. MSF 2013;773–774:119–29. https://doi.org/10.4028/www.scientific.net/MSF.773-774.119.
[41] Katajarinne T, Louhenkilpi S, Kivivuori S. A novel approach to control the properties of austenitic stainless steels in incremental forming. Materials Science and Engineering: A 2014;604:23–6. https://doi.org/10.1016/j.msea.2014.03.020.
[42] Olson G, Cohen M. Kinetics of Strain-Induced Martensitic Nucleation. Metall Trans A 1975;6:791–5. https://doi.org/10.1007/BF02672301.
[43] Angel T. Formation of Martensite in Austenitic Stainless Steels, Effect of Deformation, Temperature and Composition. Journal of the Iron and Steel Institute 1954;177:165–74.
[44] Stringfellow RG, Parks DM, Olson GB. A constitutive model for transformation plasticity accompanying strain-induced martensitic transformations in metastable austenitic steels. Acta Metallurgica et Materialia 1992;40:1703–16. https://doi.org/10.1016/0956-7151(92)90114-T.
[45] Olson G, Cohen M. Kinetics of Strain-Induced Martensitic Nucleation. Metall Trans A 1975;6:791–5. https://doi.org/10.1007/BF02672301.
[46] Young C-C. Transformation Toughening in Phosphocarbide-Strengthened Austenitic Steels. Massachusetts Institute of Technology, 1988.
[47] Tomita Y, Iwamoto T. Constitutive modeling of trip steel and its application to the improvement of mechanical properties. International Journal of Mechanical Sciences 1995;37:1295–305. https://doi.org/10.1016/0020-7403(95)00039-Z.
[48] Beese AM, Mohr D. Effect of stress triaxiality and Lode angle on the kinetics of strain-induced austenite-to-martensite transformation. Acta Materialia 2011;59:2589–600. https://doi.org/10.1016/j.actamat.2010.12.040.
[49] Raghavan KS, Thomas G, Arnold J, Gill A, Gnäupel-Herold T. A comparison of different measurement methods to evaluate strain-induced martensite formation in a metastable austenitic stainless steel. Materials Science and Technology Conference and Exhibition 2014, MS and T 2014 2014;1:187–99.

[50] Staib W, Künzel H. In-situ Ferrite Content Measurement of Duplex Steel Structures in the Chemical Industry. Practical Applications of the Alternating Field, Magnetoinductive Method. In: Höller P, Hauk V, Dobmann G, Ruud CO, Green RE, editors. Nondestructive Characterization of Materials, Berlin, Heidelberg: Springer; 1989, p. 614–21. https://doi.org/10.1007/978-3-642-84003-6_73.
[51] Helmut Fischer GmbH. Operators Manual Feritscope FMP30 2008.
[52] Talonen J, Aspegren P, Hänninen H. Comparison of Different Methods for Measuring Strain Induced Martensite Content in Austenitic Steels. Materials Science and Technology 2004;20:1506–12. https://doi.org/10.1179/026708304X4367.
[53] Beese AM, Mohr D. Identification of the Direction-Dependency of the Martensitic Transformation in Stainless Steel Using In Situ Magnetic Permeability Measurements. Exp Mech 2011;51:667–76. https://doi.org/10.1007/s11340-010-9374-y.
[54] ASTM. ASTM E8/E8M-16a Standard Test Methods for Tension Testing of Metallic Materials. ASTM Standards 2013;03.01. https://doi.org/10.1520/E0008-04.
[55] ISO 6892-1:2019. Metallic materials — Tensile testing — Part 1: Method of test at room temperature. 2019.
[56] Kalpakjian S. Manufacturing Processes for Engineering Materials (3rd Edition). USA: Addison-wesley; 1996.
[57] ISO 16808:2022. Metallic materials — Sheet and strip — Determination of biaxial stress-strain curve by means of bulge test with optical measuring systems. ISO; 2022.
[58] DIN 51524-2. Pressure fluids - Hydraulic oils - Part 2: HLP hydraulic oils, Minimum requirements. European Standards; 2017.
[59] Yin Q. Verfestigungs- und Schädigungsverhalten von Blechwerkstoffen im ebenen Torsionsversuch. 2014. https://doi.org/10.17877/DE290R-438.
[60] Stiebert F, Traphöner H, Meya R, Tekkaya AE. Characterization of Flow Curves for Ultra-Thin Steel Sheets With the In-Plane Torsion Test. J Manuf Sci Eng 2022;144:031011. https://doi.org/10.1115/1.4051919.
[61] Luo C, Yuan H. Measurement and modeling of deformation-induced martensitic transformation in a metastable austenitic stainless steel under cyclic loadings. Acta Materialia 2022;238:118202. https://doi.org/10.1016/j.actamat.2022.118202.
[62] Ha J, Lee J, Kim JH, Barlat F, Lee M. Meso-Scopic Analysis of Strain Path Change Effect on the Hardening Behavior of Dual-Phase Steel. Steel Research Int 2014;85:1047–57. https://doi.org/10.1002/srin.201300186.
[63] Ha J, Lee J, Kim JH, Lee M-G, Barlat F. Investigation of plastic strain rate under strain path changes in dual-phase steel using microstructure-based modeling. International Journal of Plasticity 2017;93:89–111. https://doi.org/10.1016/j.ijplas.2017.02.005.
[64] Feng Z, Mamros EM, Ha J, Kinsey BL, Knezevic M. Modeling of plasticity-induced martensitic transformation to achieve hierarchical, heterogeneous, and tailored microstructures in stainless steels. CIRP Journal of Manufacturing Science and Technology 2021;33:389–97. https://doi.org/10.1016/j.cirpj.2021.04.006.
[65] Mamros EM, Kuijer MB, Davarpanah MA, Baker I, Kinsey BL. The Effect of Temperature on the Strain-Induced Austenite to Martensite Transformation in SS 316L During Uniaxial Tension. In: Daehn G, Cao J, Kinsey B, Tekkaya E, Vivek A, Yoshida Y, editors. Forming the Future, Cham: Springer International Publishing; 2021, p. 1853–62. https://doi.org/10.1007/978-3-030-75381-8_155.
[66] Mamros EM, Mayer SM, Banerjee DK, Iadicola MA, Kinsey BL, Ha J. Plastic Anisotropy Evolution of SS316L and Modeling for Novel Cruciform Specimen. Int J Mech Sci 2022;234. https://doi.org/10.1016/j.ijmecsci.2022.107663.

[67] Santacreu P-O, Glez J-C, Chinouilh G, Fröhlich T. Behaviour Model of Austenitic Stainless Steels for Automotive Structural Parts. Steel Research International 2006;77:686–91. https://doi.org/10.1002/srin.200606448.
[68] Kim H, Lee J, Barlat F, Kim D, Lee M-G. Experiment and modeling to investigate the effect of stress state, strain and temperature on martensitic phase transformation in TRIP-assisted steel. Acta Materialia 2015;97:435–44. https://doi.org/10.1016/j.actamat.2015.06.023.
[69] Wang Z, Beese AM. Stress state-dependent mechanics of additively manufactured 304L stainless steel: Part 1 – characterization and modeling of the effect of stress state and texture on microstructural evolution. Materials Science and Engineering: A 2019;743:811–23. https://doi.org/10.1016/j.msea.2018.11.094.
[70] Castrol Iloform PN 226 Datasheet 2008.
[71] Hibbitt D, Karlsson B, Sorensen P. Abaqus 1978.
[72] Maaß F, Hahn M, Tekkaya AE. Setting Residual Stresses in Tensile Stress-superposed Incremental Sheet Forming. Proceedings of the 22nd International Conference on Material Forming, 2022.
[73] Moser N, Leem D, Ehmann K, Cao J. A high-fidelity simulation of double-sided incremental forming: Improving the accuracy by incorporating the effects of machine compliance. Journal of Materials Processing Technology 2021;295:117152.
[74] Maker BN. Input Parameters for Metal Forming Simulation Using LS-DYNA 2001.
[75] Barlat F, Gracio JJ, Lee M-G, Rauch EF, Vincze G. An alternative to kinematic hardening in classical plasticity. International Journal of Plasticity 2011;27:1309–27. https://doi.org/10.1016/j.ijplas.2011.03.003.
[76] Barlat F, Ha JJ, Gracio JJ, Lee MG, Rauch EF, Vincze G. Extension of homogeneous anisotropic hardening model to cross-loading with latent effects. International Journal of Plasticity 2013;46:130–42. https://doi.org/10.1016/j.ijplas.2012.07.002.
[77] Lee J, Bong HJ, Ha J, Choi J, Lee M-G, Barlat F. Influence of Yield Stress Determination in Anisotropic Hardening Model on Springback Prediction in Dual-Phase Steel. JOM 2018;70. https://doi.org/10.1007/s11837-018-2910-4.
[78] Chaboche JL, Van KD, Cordier G. Modelization of the Strain Memory Effect on the Cyclic Hardening of 316 Stainless Steel 1979.
[79] Yoshida F, Uemori T, Fujiwara K. Elastic–plastic behavior of steel sheets under in-plane cyclic tension–compression at large strain. International Journal of Plasticity 2002;18:633–59. https://doi.org/10.1016/S0749-6419(01)00049-3.
[80] Carette Y, Vanhulst M, Duflou JR. Geometry Compensation Methods for Increasing the Accuracy of the SPIF Process. Key Engineering Materials 2021;883:217–24. https://doi.org/10.4028/www.scientific.net/KEM.883.217.
[81] Al-Ghamdi K, Hussain G. The pillowing tendency of materials in single-point incremental forming: Experimental and finite element analyses. Proceedings of the Institution of Mechanical Engineers, Part B: Journal of Engineering Manufacture 2015;229:744–53. https://doi.org/10.1177/0954405414530906.
[82] Fathi H, Semnani HRM, Emadoddin E, Sadeghi BM. Effect of martensitic transformation on springback behavior of 304L austenitic stainless steel. Mater Res Express 2017;4:096510. https://doi.org/10.1088/2053-1591/aa89f8.
[83] Jackson K, Allwood J. The mechanics of incremental sheet forming. Journal of Materials Processing Technology 2009;209:1158–74. https://doi.org/10.1016/j.jmatprotec.2008.03.025.
[84] Ambrož O, Mikmeková Š, Hegrová V, Aoyama T. TRIP Steel Specimen Preparation for Advanced SEM and EBSD, 2020, p. 518–22. https://doi.org/10.37904/metal.2020.3513.
[85] Jägle D-IEA. Modelling of Microstructural Banding during Transformations in Steel Dipl, 2007.

[86] Stauffer AC, Koss DA, McKirgan JB. Microstructural banding and failure of a stainless steel. Metall Mater Trans A 2004;35:1317–24. https://doi.org/10.1007/s11661-004-0306-2.
[87] Darzi S, Adams MD, Roth JT, Kinsey BL, Ha J. Manipulating Martensite Transformation of SS304L During Double-Sided Incremental Forming by Varying Temperature and Deformation Path. CIRP Annals Manufacturing Technology 2023.